2018

Isostructural metal-insulator transition in VO2

D. Lee, B. Chung, Y. Shi, G.-Y. Kim, N. Campbell, F. Xue, K. Song, S.-Y. Choi, J. P. Podkaminer, T. H. Kim, P. J. Ryan, J.-W. Kim, T. R. Paudel, J.-H. Kang, J. W. Spinuzzi, D. A. Tenne, E. Y. Tsymbal, M. S. Rzchowski, L. Q. Chen, J. Lee, and C. B. Eom

SOLID-STATE PHYSICS

Isostructural metal-insulator transition in VO_2

D. Lee[1], B. Chung[2], Y. Shi[3], G.-Y. Kim[4]*, N. Campbell[5], F. Xue[3], K. Song[4], S.-Y. Choi[4]*, J. P. Podkaminer[1], T. H. Kim[1], P. J. Ryan[6,7], J.-W. Kim[6], T. R. Paudel[8], J.-H. Kang[1], J. W. Spinuzzi[9], D. A. Tenne[9], E. Y. Tsymbal[8], M. S. Rzchowski[5], L. Q. Chen[3], J. Lee[2]†, C. B. Eom[1]†

The metal-insulator transition in correlated materials is usually coupled to a symmetry-lowering structural phase transition. This coupling not only complicates the understanding of the basic mechanism of this phenomenon but also limits the speed and endurance of prospective electronic devices. We demonstrate an isostructural, purely electronically driven metal-insulator transition in epitaxial heterostructures of an archetypal correlated material, vanadium dioxide. A combination of thin-film synthesis, structural and electrical characterizations, and theoretical modeling reveals that an interface interaction suppresses the electronic correlations without changing the crystal structure in this otherwise correlated insulator. This interaction stabilizes a nonequilibrium metallic phase and leads to an isostructural metal-insulator transition. This discovery will provide insights into phase transitions of correlated materials and may aid the design of device functionalities.

Understanding metal-insulator transitions in strongly correlated materials is one of the major challenges in condensed matter physics (*1*–*5*), with implications for both fundamental science and technology (*6*, *7*). Correlated materials exhibit strong coupling between charge, spin, and lattice degrees of freedom, so that the metal-insulator transition is almost always accompanied by an associated structural phase transition. This coexistence obscures the underlying physics, making it difficult to disentangle the different intrinsic interactions controlling the metal-insulator transition. Furthermore, the structural transition generally limits the ultimate switching speed (*8*, *9*) and endurance (*6*, *10*) of ultrafast electronic devices (*6*, *7*, *11*) based on the metal-insulator transition in these correlated materials. Achieving an isostructural metal-insulator transition is thus of great interest.

As a model system for this study, we chose the archetypal correlated material vanadium dioxide (VO_2) (*12*–*27*). VO_2 is metallic at high temperatures and becomes insulating near room temperature (341 K in bulk) (*12*); the metal-insulator transition is accompanied by a structural phase transition from the high-temperature rutile structure to the low-temperature monoclinic structure via the formation of V-V dimers along the *c* axis. There has been extensive debate over whether the primary mechanism of the metal-insulator transition in VO_2 is an electron-lattice interaction (Peierls transition) (*13*) or an electron-electron interaction (Mott transition) (*14*), and it is now accepted that both Peierls and Mott physics are important (*15*, *16*). In particular, recent ultrafast photoexcitation experiments (*21*, *22*) have revealed the presence of a nonequilibrium metallic monoclinic state in addition to the known bulk equilibrium phases (i.e., insulating monoclinic and metallic rutile phases). This metallic transition in photoexcited monoclinic VO_2 could originate from the dynamically screened Coulomb interaction (*22*), assisted by an electronically one-dimensional characteristic of V-V dimers (*27*), and suggests a route for an isostructural metal-insulator transition: If the metallic monoclinic phase could be stabilized, rather than just being transient, we could achieve an isostructural metallic transition in insulating monoclinic VO_2.

To this end, we considered a nanoscale bilayer consisting of two VO_2 layers with different transition temperatures (T_1 and T_2 in Fig. 1A). In this bilayer, a rutile/monoclinic heterostructure can occur at intermediate temperatures between T_1 and T_2, in which interval the desired metallic monoclinic phase might be stabilized (e.g., via a collective carrier delocalization) (*19*). To experimentally realize such a bilayer, we needed to achieve control over the transition temperature in a VO_2 layer; to do that, we used an intrinsic point defect (i.e., oxygen vacancy) (*28*) and the resulting electron doping. Introducing a minute amount of oxygen vacancies can lower the transition temperature of VO_2 without compromising the sharp metal-insulator transition (*29*). By changing the oxygen partial pressure during film growth (figs. S1 to S4) (*30*), we prepared an artificial bilayer (Fig. 1B, inset), fully coherent on TiO_2 (001) substrate, consisting of slightly oxygen-deficient $VO_{2-\delta}$ and stoichiometric VO_2 layers. The individual 8-nm-thick $VO_{2-\delta}$ and VO_2 layers have transition temperatures of T_1 ~ 279 K and T_2 ~ 287 K, respectively (Fig. 1A).

To visualize the oxygen vacancy profile in the bilayer, we carried out atomic-scale imaging using scanning transmission electron microscopy (STEM) (*30*). In STEM, the low-angle annular dark field (LAADF) image is very sensitive to the strain fields from oxygen vacancies (*28*), whereas the high-angle annular dark field (HAADF) image is dominated by the (high-Z) cation sites (Fig. 1B). The HAADF image shows little intensity change across the $VO_{2-\delta}/VO_2$ interface (denoted by the white dashed line). In contrast, the LAADF image displays a noticeable, abrupt intensity change across the $VO_{2-\delta}/VO_2$ interface, emphasizing the oxygen deficiency in the $VO_{2-\delta}$ layer. Our results show

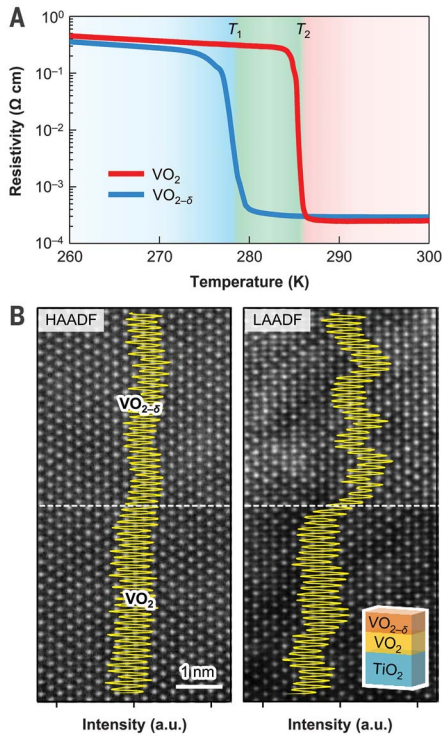

Fig. 1. Design of an artificial $VO_{2-\delta}/VO_2$ bilayer. (**A**) Electrical resistivity measured as a function of temperature of 8-nm-thick epitaxial VO_2 and $VO_{2-\delta}$ single-layer films on (001) TiO_2 substrates. The oxygen vacancy concentration δ is roughly estimated as δ ~ 0.01 (fig. S3). (**B**) HAADF- and LAADF-STEM images of the $VO_{2-\delta}/VO_2$ bilayer (inset) projected along [100]. Yellow lines show the average line profile of the HAADF (left) and LAADF (right) image intensities. White dashed lines represent a nominal interface between VO_2 and $VO_{2-\delta}$.

[1]Department of Materials Science and Engineering, University of Wisconsin, Madison, WI 53706, USA. [2]School of Advanced Materials Science and Engineering, Sungkyunkwan University, Suwon 16419, Korea. [3]Department of Materials Science and Engineering, Pennsylvania State University, University Park, PA 16802, USA. [4]Department of Materials Modeling and Characterization, Korea Institute of Materials Science, Changwon 642-831, Korea. [5]Department of Physics, University of Wisconsin, Madison, WI 53706, USA. [6]Advanced Photon Source, Argonne National Laboratory, Argonne, IL 60439, USA. [7]School of Physical Sciences, Dublin City University, Dublin 9, Ireland. [8]Department of Physics and Astronomy and Nebraska Center for Materials and Nanoscience, University of Nebraska, Lincoln, NE 68588, USA. [9]Department of Physics, Boise State University, Boise, ID 83725, USA.
*Present address: Department of Materials and Science, POSTECH, Pohang 37673, Korea.
†Corresponding author. Email: eom@engr.wisc.edu (C.B.E.); jclee@skku.edu (J.L.)

that introducing a small amount of oxygen vacancies, rather than extrinsic dopants, creates a chemically sharp interface with a sub–1-nm width (fig. S5) and leads to a quasi-homogeneous, single-crystalline character of the bilayer. Electron energy loss spectroscopy (EELS) measurements (fig. S6) independently quantified the oxygen vacancy difference between the layers. Considering this nanoengineered oxygen vacancy profile, we expect two distinct transition temperatures in the top $VO_{2-\delta}$ and bottom VO_2 layers.

Using Raman spectroscopy (*30*), we monitored the structural phase transition in the $VO_{2-\delta}/VO_2$ bilayer (Fig. 2, A and B). With decreasing temperature, several noticeable Raman peaks (e.g., ω_1, ω_2, and ω_3 peaks in Fig. 2A) arise suddenly from the monoclinic distortions during the structural transition (*31*, *32*). Our quantitative analysis (Fig. 2B) clearly shows the two-step structural phase transition in the $VO_{2-\delta}/VO_2$ bilayer, contrary to the single-step transition in a VO_2 single layer. Using temperature-dependent x-ray diffraction measurements (Fig. 2, C to E) (*30*) and phase-field simulations (fig. S14), we confirmed the two-step structural phase transition in the bilayer. This two-step structural phase transition can be explained by two separate structural transitions: at $T \sim 279$ K for the top $VO_{2-\delta}$ layer, and at $T \sim 287$ K for the bottom VO_2 layer. At intermediate temperatures between $T \sim 279$ K and 287 K (Fig. 2, B and E, green), the top $VO_{2-\delta}$ and bottom VO_2 layers have rutile and monoclinic structures, respectively, which together form the desired rutile/monoclinic heterostructure (Fig. 2B, inset).

We explored the electronic phase transition in the $VO_{2-\delta}/VO_2$ bilayer by measuring the electrical resistivity (Fig. 3A) and carrier concentration (fig. S7). In stark contrast to the two-step structural transition, our bilayer showed a single-step, collective metal-insulator transition at $T \sim 279$ K. The electronic phase transition of the bilayer looked nearly identical to that of a $VO_{2-\delta}$ single layer (Fig. 3A, black dashed line), which means that in the $VO_{2-\delta}/VO_2$ bilayer, the electronic phase (i.e., metallic or insulating) of the VO_2 layer collectively follows that of the $VO_{2-\delta}$ layer. Notably, when an ultrathin (~2 nm) TiO_2 layer was inserted between $VO_{2-\delta}$ and VO_2, the $VO_{2-\delta}/TiO_2/VO_2$ system exhibited a two-step metal-insulator transition (fig. S8). This confirms the intrinsic effect of the rutile/monoclinic interface on the observed single-step, collective metal-insulator transition in the $VO_{2-\delta}/VO_2$ bilayer.

Taken together, our observations of the two-step structural and single-step electronic phase transitions unambiguously confirm the emergence of a stable metallic monoclinic phase in the $VO_{2-\delta}/VO_2$ bilayer. With the decrease in temperature, the bottom VO_2 layer exhibited the rutile-to-monoclinic structural transition at $T \sim 287$ K (Fig. 3B), but the global metallicity of the whole bilayer remained unchanged (Fig. 3A and fig. S7). This is consistent with the explanation that, when interfaced with the metallic rutile $VO_{2-\delta}$ layer, the bottom VO_2 layer becomes a stable metallic monoclinic phase. This interface-induced bulk carrier delocalization (*19*) plays a decisive role in the single-step metal-insulator transition. Figure 3C shows little change in the peak positions of ω_2 and ω_3, attributed to the ionic motion of V-V dimers (*23*, *32*), during the metal-insulator transition at ~279 K. This directly illustrates the isostructural metal-insulator transition without any crystalline structure change at ~279 K in the bottom stoichiometric VO_2 layer.

To further understand the emergence of isostructural metal-insulator transition, we carried out theoretical modeling of the rutile/monoclinic heterostructure. First, we performed non–spin-polarized density functional theory (DFT) calculations (*30*) with Hubbard U correction for properly predicting the insulating monoclinic ground state in bulk VO_2 (*33*). The calculated density of states of the heterostructure (Fig. 4A) manifested the metallic nature in the monoclinic region (Fig. 4B and fig. S10), consistent with our experimental observation (Fig. 3). Inside the monoclinic region, the electronic structure was strongly modified, resulting in noticeable band gap narrowing. This was largely driven by hole doping of the monoclinic region (fig. S12), stemming from the different work functions of the rutile and monoclinic phases (*34*). Such a hole doping reduces electronic correlations, causing a complete collapse of the band gap in monoclinic VO_2 (*22*). Simultaneously, from the DFT results, we infer that the rutile/monoclinic heterostructure has a very small interfacial energy (*30*), which may also play a role in stabilizing the metallic monoclinic phase.

To explore the effects of electronic correlations and interfacial energy, we used a generalized Landau thermodynamic approach implemented

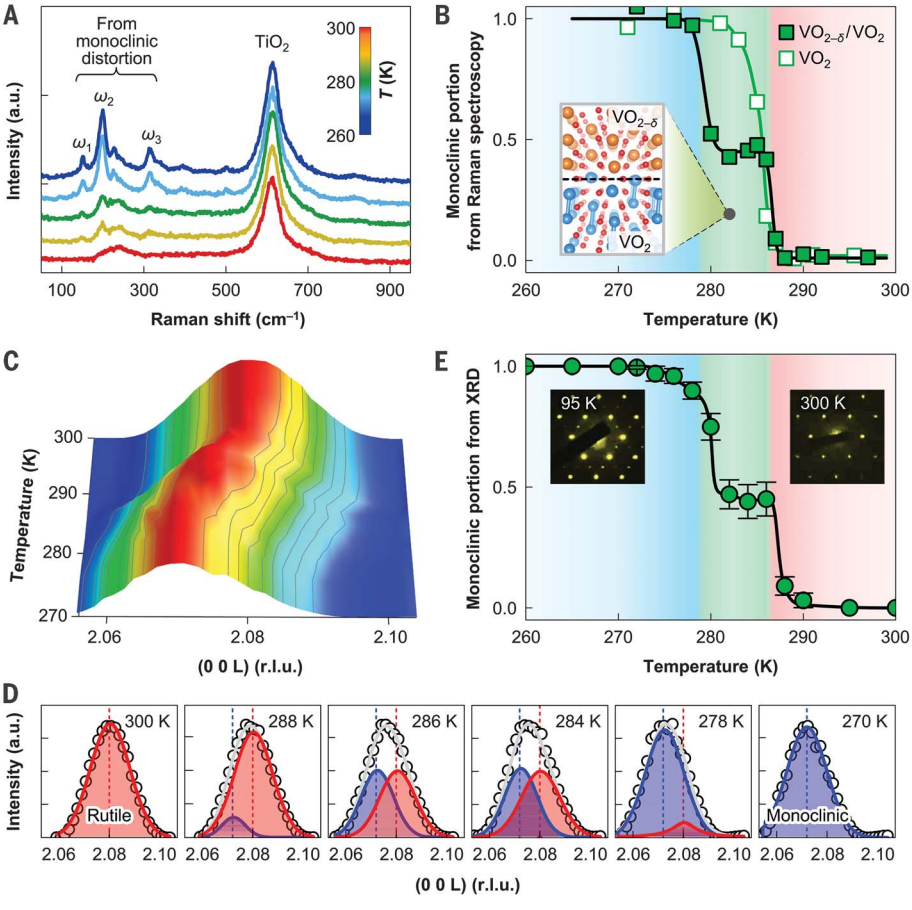

Fig. 2. Structural phase transition in the $VO_{2-\delta}/VO_2$ bilayer. (**A**) Raman spectra of $VO_{2-\delta}$ (8 nm)/VO_2 (8 nm) bilayer at various temperatures. Raman peaks from the monoclinic distortion are denoted ω_1, ω_2, and ω_3; a.u., arbitrary units. (**B**) Relative monoclinic portion as a function of temperature, estimated from monoclinic Raman intensity in (A). Inset: Schematic of atomic structure of $VO_{2-\delta}/VO_2$ bilayer at intermediate temperatures. (**C**) X-ray diffraction (XRD) (00L) scans of $VO_{2-\delta}/VO_2$ bilayer, measured upon cooling. (**D**) Representative XRD peaks at several temperatures. Red and blue vertical dashed lines indicate the XRD peak positions for rutile ($L \sim 2.080$) and monoclinic ($L \sim 2.072$) phases, respectively. We fit the measured XRD data (open circles) with a sum (gray curve) of two Gaussian curves with the peaks at $L \sim 2.080$ (red curve) and $L \sim 2.072$ (blue curve). (**E**) Relative monoclinic portion as a function of temperature, estimated from XRD peak analysis in (D). Error bars denote SD of the fitted peak area. Insets show the measured electron diffraction patterns of the bilayer at low and high temperatures.

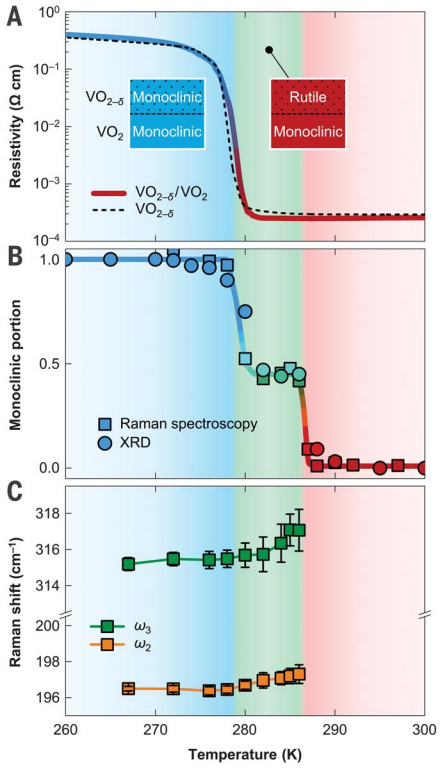

Fig. 3. Isostructural metal-insulator transition in the $VO_{2-\delta}/VO_2$ bilayer. (**A**) Electrical resistivity versus temperature of $VO_{2-\delta}$ (8 nm)/VO_2 (8 nm) bilayer (solid line) and 8-nm-thick $VO_{2-\delta}$ single layer (black dashed line), measured upon cooling. Metallic and insulating phases are represented by red and blue colors, respectively. (**B**) Monoclinic portion (from Fig. 2, B and E) as a function of temperature. (**C**) Temperature dependence of monoclinic Raman shift (i.e., ω_2 and ω_3 in Fig. 2A). Error bars denote SD of the fitted Raman peak position. We fit the measured Raman peak with a Gaussian curve.

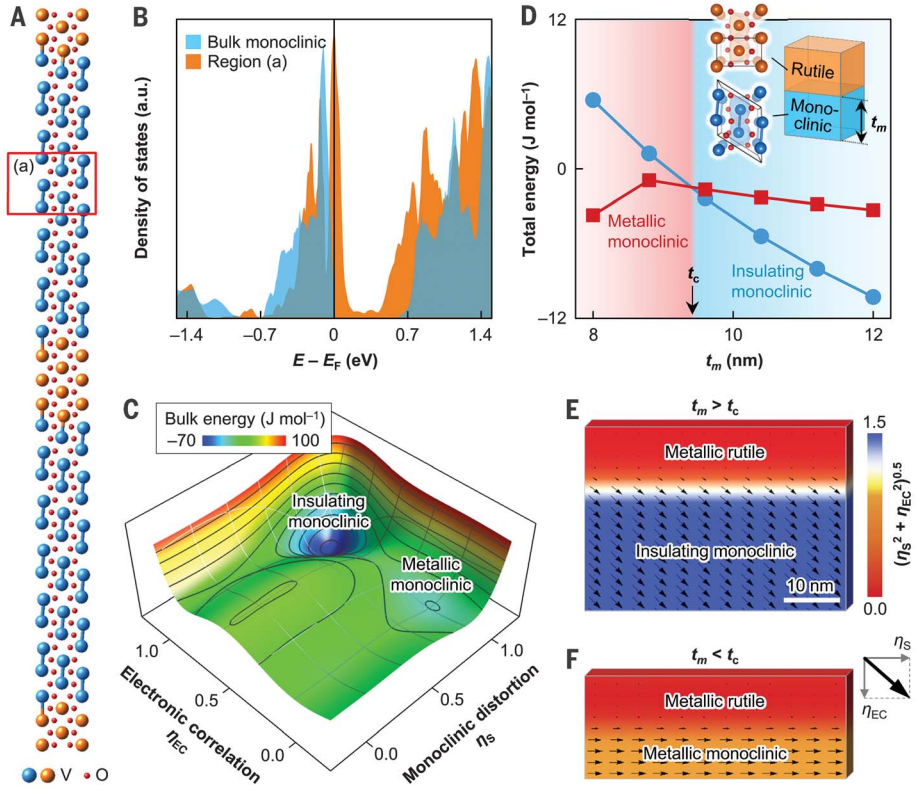

Fig. 4. Theoretical modeling of the metallic monoclinic VO_2 phase. (**A**) The rutile/monoclinic heterostructure used in the DFT calculation (*30*). V atoms are shown in two colors: orange for rutile VO_2 and blue for monoclinic VO_2. (**B**) The calculated density of states of the local monoclinic region [denoted by (a) in (A)] in the rutile/monoclinic heterostructure shows a metallic nature, distinct from the insulating nature of the bulk monoclinic VO_2 (blue). (**C**) Free energy landscape of bulk VO_2 at 287 K, just below the transition temperature. (**D**) Total energies as a function of t_m in the rutile/monoclinic heterostructure. t_c is estimated to be ~9.4 nm. (**E** and **F**) Stable states of the rutile/monoclinic heterostructure for $t_m > t_c$ (E) and $t_m < t_c$ (F). The arrows represent the two-component order parameter (η_S, η_{EC}); the color represents the norm $(\eta_S^2 + \eta_{EC}^2)^{0.5}$.

in phase-field modeling (*30*). The Landau potential incorporates two different order parameters: η_S, describing the structural transition [i.e., from rutile ($\eta_S = 0$) to monoclinic ($\eta_S = 1$) phase], and η_{EC}, describing the electronic correlations, which control the metal-insulator transition [i.e., from metal ($\eta_{EC} = 0$) to insulator ($\eta_{EC} = 1$)]. We found only two bulk equilibrium phases: the metallic rutile phase with little electronic correlation ($\eta_S = \eta_{EC} = 0$) at high temperatures, and the correlated insulating monoclinic phase ($\eta_S = \eta_{EC} = 1$) at low temperatures (fig. S13). However, in addition to these bulk equilibrium phases, we predict the presence of a nonequilibrium metallic monoclinic phase with suppressed correlation ($\eta_S = 1$ and $\eta_{EC} = 0$), as represented by the local minimum in the energy landscape just below the transition temperature (Fig. 4C).

We then used phase-field modeling to investigate phase stabilities in the experimentally studied rutile/monoclinic heterostructure. Figure 4D shows the total energy of the rutile/monoclinic heterostructure as a function of the thickness t_m of the monoclinic layer. The interfacial energy between metallic rutile and metallic monoclinic phases is naturally smaller than that between metallic rutile and insulating monoclinic phases in the phase-field model, owing to the homogeneous η_{EC} in the former case (*30*). When t_m is below critical thickness t_c, the interfacial energy contribution dominates over the bulk energy contribution, and as a result, the metallic monoclinic phase with suppressed correlation (i.e., $\eta_{EC} = 0$) becomes energetically preferred and stabilized (fig. S14). It is noteworthy that our experimental and theoretical results have consistently demonstrated the isostructural metal-insulator transition in device-relevant thin-film geometries of genuine VO_2, without the necessity of specific conditions, such as ultrafast photoexcitation (*21*, *22*), high pressure (*23*), or suppression of structural distortion at the surface (*5*, *25*). Stabilizing the monoclinic structure through our bilayer approach separates the electronic and structural phase transitions, in contrast to previous reports (*35*, *36*).

There has been a growing interest in nonequilibrium states in correlated materials (*21*, *22*, *37*), because of the opportunity to discover exotic physics not exhibited in equilibrium. Ultrafast spectroscopies have been mainly used for exploring nonequilibrium states; our study paves a way to stabilize and explore the nonequilibrium phase (e.g., metallic monoclinic state in VO_2) in a controlled way. Because VO_2 is a simple spin-½ system with one *d* electron (*38*), it will be intriguing to study the spin and orbital physics in the stabilized metallic monoclinic phase. We anticipate that our approach for artificial stabilization of nonequilibrium states will be generally applicable to correlated materials, so that a variety of unconventional phenomena can be designed through heterostructure engineering.

REFERENCES AND NOTES

1. M. Imada, A. Fujimori, Y. Tokura, *Rev. Mod. Phys.* **70**, 1039 (1998).
2. M. Uehara, S. Mori, C. H. Chen, S.-W. Cheong, *Nature* **399**, 560–563 (1999).
3. L. Zhang, C. Israel, A. Biswas, R. L. Greene, A. de Lozanne, *Science* **298**, 805–807 (2002).

4. E. Dagotto, *Science* **309**, 257–262 (2005).
5. R. G. Moore *et al*., *Science* **318**, 615–619 (2007).
6. Z. Yang, C. Ko, S. Ramanathan, *Annu. Rev. Mater. Res.* **41**, 337–367 (2011).
7. D. M. Newns *et al*., *Appl. Phys. Lett.* **73**, 780–782 (1998).
8. A. Cavalleri, Th. Dekorsy, H. H. W. Chong, J. C. Kieffer, R. W. Schoenlein, *Phys. Rev. B* **70**, 161102(R) (2004).
9. P. Baum, D.-S. Yang, A. H. Zewail, *Science* **318**, 788–792 (2007).
10. D. Maurer, A. Leue, *Mater. Sci. Eng. A* **370**, 440–443 (2004).
11. Y. Zhou, S. Ramanathan, *Proc. IEEE* **103**, 1289–1310 (2015).
12. F. J. Morin, *Phys. Rev. Lett.* **3**, 34–36 (1959).
13. R. M. Wentzcovitch, W. W. Schulz, P. B. Allen, *Phys. Rev. Lett.* **72**, 3389–3392 (1994).
14. T. M. Rice, H. Launois, J. P. Pouget, *Phys. Rev. Lett.* **73**, 3042 (1994).
15. S. Biermann, A. Poteryaev, A. I. Lichtenstein, A. Georges, *Phys. Rev. Lett.* **94**, 026404 (2005).
16. M. W. Haverkort *et al*., *Phys. Rev. Lett.* **95**, 196404 (2005).
17. M. M. Qazilbash *et al*., *Science* **318**, 1750–1753 (2007).
18. M. Liu *et al*., *Nature* **487**, 345–348 (2012).
19. M. Nakano *et al*., *Nature* **487**, 459–462 (2012).
20. J. Jeong *et al*., *Science* **339**, 1402–1405 (2013).
21. V. R. Morrison *et al*., *Science* **346**, 445–448 (2014).
22. D. Wegkamp *et al*., *Phys. Rev. Lett.* **113**, 216401 (2014).
23. E. Arcangeletti *et al*., *Phys. Rev. Lett.* **98**, 196406 (2007).
24. Z. Tao *et al*., *Phys. Rev. Lett.* **109**, 166406 (2012).
25. J. Laverock *et al*., *Phys. Rev. Lett.* **113**, 216402 (2014).
26. J. D. Budai *et al*., *Nature* **515**, 535–539 (2014).
27. V. Eyert, *Ann. Phys.* **11**, 650–704 (2002).
28. D. A. Muller, N. Nakagawa, A. Ohtomo, J. L. Grazul, H. Y. Hwang, *Nature* **430**, 657–661 (2004).
29. C. H. Griffiths, H. K. Eastwood, *J. Appl. Phys.* **45**, 2201–2206 (1974).
30. See supplementary materials.
31. R. Srivastava, L. L. Chase, *Phys. Rev. Lett.* **27**, 727–730 (1971).
32. L. Bai *et al*., *Phys. Rev. B* **91**, 104110 (2015).
33. X. Yuan, Y. Zhang, T. A. Abtew, P. Zhang, W. Zhang, *Phys. Rev. B* **86**, 235103 (2012).
34. C. Ko, Z. Yang, S. Ramanathan, *ACS Appl. Mater. Interfaces* **3**, 3396–3401 (2011).
35. M. Yang *et al*., *Sci. Rep.* **6**, 23119 (2016).
36. The supplementary x-ray data in (*35*) indicate that a structural transition remains.
37. J. Kim *et al*., *Science* **346**, 1205–1208 (2014).
38. H. He *et al*., *Phys. Rev. B* **94**, 161119(R) (2016).

ACKNOWLEDGMENTS

Funding: Supported by the NSF under DMREF grant DMR-1629270, AFOSR grant FA9550-15-1-0334, and Office of Naval Research N00014-13-1-0183. Transport measurement at the University of Wisconsin–Madison was supported by the U.S. Department of Energy (DOE), Office of Science, Office of Basic Energy Sciences (BES), under award DE-FG02-06ER46327. The work at Sungkyunkwan University was supported by National Research Foundation of Korea through the Basic Research Program (2009-0092809) and KISTI supercomputing center (KSC-2015-C3-067). The work at Penn State is also partially supported by the NSF MRSEC under grant DMR-1420620 (Y.S.). S.Y.C. and G.Y.K. acknowledge the support the Global Frontier Hybrid Interface Materials of the NRF funded by Korea Government (2013M3A6B1078872). K.S. acknowledges the Fundamental Research Program of the Korean Institute of Materials Science (PNK5570). The research at the University of Nebraska–Lincoln is supported by NSF through the Nebraska Materials Science and Engineering Center (MRSEC grant DMR-1420645). Use of the Advanced Photon Source, an Office of Science User Facility operated for the U.S. DOE Office of Science by Argonne National Laboratory, was supported by the DOE under contract DE-AC02-06CH11357. **Author contributions:** D.L. and C.B.E. conceived the project; C.B.E., M.S.R., and D.A.T. supervised the experiments; J.L., L.Q.C., and E.Y.T. supervised the theoretical calculations; D.L., J.P.P., and C.B.E. fabricated thin films and performed structural characterization; B.C., T.R.P., E.Y.T., and J.L. performed density functional theory calculations; Y.S., F.X., and L.Q.C. performed phase-field simulations; G.-Y.K., K.S., and S.-Y.C. performed scanning transmission electron microscopy experiments; N.C., T.H.K., J.-H.K., and M.S.R. performed transport measurements; P.J.R. and J.-W.K. performed temperature-dependent x-ray diffraction experiments; J.W.S. and D.A.T. performed Raman spectroscopy experiments; D.L., J.L., L.Q.C., M.S.R., E.Y.T., and C.B.E. prepared the manuscript; and C.B.E. directed the overall research. **Competing interests:** D.L. and C.B.E. are co-inventors on a U.S. patent application based on the results of this work filed by the University of Wisconsin–Madison. **Data and materials availability:** For our DFT calculations, we used VASP, a commercial software package (www.vasp.at/). All data are available in the manuscript or the supplementary materials.

SUPPLEMENTARY MATERIALS

www.sciencemag.org/content/362/6418/1037/suppl/DC1
Materials and Methods
Figs. S1 to S14
Table S1
Data S1
References (*39*–*59*)

17 February 2017; resubmitted 28 September 2017
Accepted 12 October 2018
10.1126/science.aam9189

Science

Isostructural metal-insulator transition in VO_2

D. Lee, B. Chung, Y. Shi, G.-Y. Kim, N. Campbell, F. Xue, K. Song, S.-Y. Choi, J. P. Podkaminer, T. H. Kim, P. J. Ryan, J.-W. Kim, T. R. Paudel, J.-H. Kang, J. W. Spinuzzi, D. A. Tenne, E. Y. Tsymbal, M. S. Rzchowski, L. Q. Chen, J. Lee and C. B. Eom

Science **362** (6418), 1037-1040.
DOI: 10.1126/science.aam9189

Separating structure and electrons in VO_2

Above 341 kelvin—not far from room temperature—bulk vanadium dioxide (VO_2) is a metal. But as soon as the material is cooled below 341 kelvin, VO_2 turns into an insulator and, at the same time, changes its crystal structure from rutile to monoclinic. Lee *et al.* studied the peculiar behavior of a heterostructure consisting of a layer of VO_2 placed underneath a layer of the same material that has a bit less oxygen. In the VO_2 layer, the structural transition occurred at a higher temperature than the metal-insulator transition. In between those two temperatures, VO_2 was a metal with a monoclinic structure—a combination that does not occur in the absence of the adjoining oxygen-poor layer.

Science, this issue p. 1037